Subjective Surfaces: A Geometric Model for Boundary Completion

A. Sarti, R. Malladi, and J. A. Sethian

Department of Mathematics
and
Lawrence Berkeley National Laboratory
University of California
Berkeley, CA 94720

Abstract

We present a geometric model and a computational method for segmentation of images with missing boundaries. In many situations, the human visual system fills in missing gaps in edges and boundaries, building and completing information that is not present. Boundary completion presents a considerable challenge in computer vision, since most algorithms attempt to exploit existing data. A large body of work concerns completion models, which postulate how to construct missing data; these models are often trained and specific to particular images. In this paper, we take the following, alternative perspective: we consider a given reference point within the image, and then develop an algorithm which tries to build missing information on the basis of the given point of view and the available information as boundary data to the algorithm. Starting from this point of view, a surface is constructed. It is then evolved with the mean curvature flow in the metric induced by the image until a piecewise constant solution is reached. We test the computational model on modal completion, amodal completion, and texture segmentation. We extend the geometric model and the algorithm to 3D in order to extract shapes from low signal/noise ratio ultrasound image volumes. Results in 3D echocardiography and 3D fetal echography are also presented.

Keywords: Subjective surfaces, Segmentation, Perceptual contours, Level sets, Differential geometry, Riemannian geometry, Surface evolution

1 Introduction

Consider the images in Figure 1. The human visual system completes the internal objects exploiting the existing sparse data. In the image on the left, a solid triangle in the center of the figure appears to have well-defined contours even in completely homogeneous areas; in the center figure, a large rectangle is perceived, and, in the figure on the right, a white square partially occluded by a gray
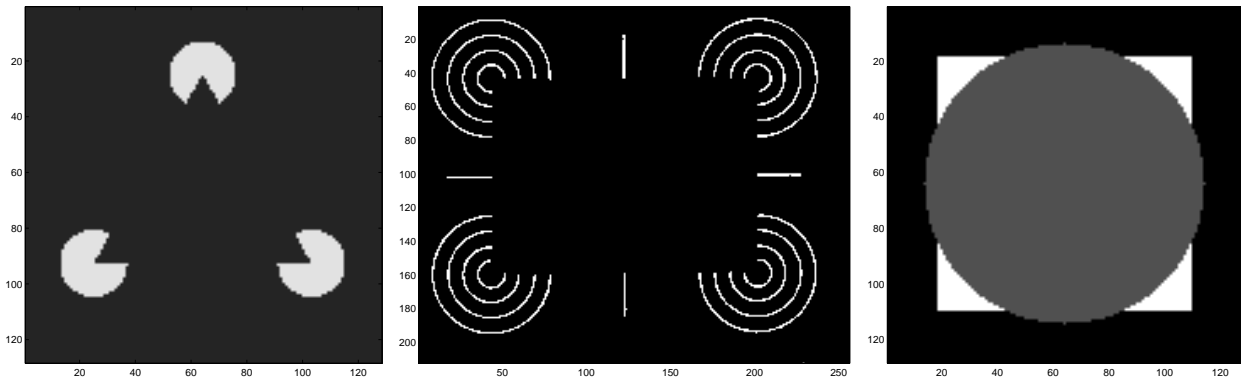
Figure 1: Three images with subjective contours.

disk is perceived. These contours, which are not characterized by image gradients, may be thought of as "apparent" or "subjective" contours. Following the usual convention, we distinguish between "modal completion", in which the goal is to construct a perceived boundary (as in Figure 1, left and center) and "amodal completion", in which one reconstructs the shape of a partially occluded objects (as in Figure 1, right); see [10, 11].

Our goal is to extract, i.e. segment, these internal objects. Since some information is missing, one class of algorithms typically complete the segmentation process by building models to postulate what happens between the available data. In this paper we present a method for segmentation of images with missing boundaries.

We take the following perspective:

- The observer is drawn to a reference point within the image, and this is a natural point from which to construct a completion process.

- Starting from this given reference point, we can devise an algorithm which takes advantage of the available boundary data to construct a complete segmentation. Thus, the computed segmentation is a function of the reference point.

As in [31], we view a segmentation as the construction of a piecewise constant surface that varies rapidly across the boundary between different objects and stays flat within it. In [25] the segmentation is a piecewise smooth/constant approximation of the image. In our approach the

2

segmentation is a piecewise constant approximation of the point-of-view or the reference surface. To obtain it we define the following steps:

1. Select a fixation point and build an initial surface corresponding to this point-of-view.

2. Detect existing local features in the image.

3. Evolve the point of view surface with a flow that depends both on the geometry of the surface and on the image features. The flow evolves the initial condition towards a piecewise constant surface. The completed object is the flat manifold at the top of the surface.

4. (Automatically) Pick the level set that describes the desired object (that is a closed curve).

During the evolution, the point-of-view surface is attracted by the existing boundaries and steepens. The surface evolves towards a piecewise constant solution through the closing of the boundary fragments and the filling in the homogeneous regions. A solid object is delineated as a constant surface bounded by existing and recovered shape boundaries. With this method, the image completion process depends both on the point of view and on the geometric properties of the image [31].

Human perceptual organization has been extensively studied, and the resulting theories of vision are often used to construct computational models for image segmentation. For example, properties like boundary continuity of direction, regularity, proximity constraints, maximum homogeneity, closure, and symmetry have been applied as guidelines for many computer vision algorithms. The perspective and algorithms in this paper are connected to some experimental results on perceptual organization of the human visual system outlined by Kanizsa [10, 11, 12]. In particular, the emergence of the subjective contours depends on the position of the point of view: "if you fix your gaze on an apparent contour, it disappears, yet if you direct your gaze to the entire figure, the contours appear to be real," see [10].

In the following, we construct a geometrical model for boundary completion by keeping in mind the aforementioned characteristics of perceptual organization. Both the mathematical and algorithmic approach in our method relies on a considerable body of recent work based on a partial differential equations approach to both front propagation and to image segmentation. Level set

methods, introduced by Osher and Sethian [28], track the evolution of curves and surfaces, using the theory of curve and surface evolution and the link between front propagation and hyperbolic conservation laws developed by Sethian in [37, 38]. These methods embed the desired interface as the zero level set of an implicit function, and then employ finite differences to approximate the solution of the resulting initial value partial differential equation. Malladi, Sethian and Vemuri [21] and Caselles, Catte, Coll, and Dibos in [1] used this technology to segment images by growing trial shapes inside a region with a propagation velocity which depends on the image gradient and hence stops when the boundary is reached; thus, image segmentation is transformed into an initial value partial differential equation in which a propagating front stops at the desired edge.

In [40], Sochen, Kimmel, and Malladi view image processing as the evolution of an image manifold embedded in a higher dimensional Riemannian space towards a minimal surface. This framework has been applied to processing both single- and vector-valued images defined in two and higher dimensions (see [14]). In this paper we view segmentation as the evolution of an initial reference manifold under the influence of local image features.

Our approach takes a more general view of the segmentation problem. Rather than follow a particular front or level curve which one attempts to steer to the desired edge (as in [21, 22, 23, 1, 2, 3]), we begin with an initial surface, chosen on the basis of a user-supplied reference fixation point. We then flow this *entire surface* under a speed law dependent on the image gradient, without regard to any particular level set. Suitably chosen, this flow sharpens the surface around the edges and connects segmented boundaries across the missing information. On the basis of this surface sharpening, we can identify a level set corresponding to an appropriate segmented edge.

In [31], the theoretical underpinnings of this approach were presented. In this paper we concentrate on results for a variety of 2D images (cognitive, medical, photographic, texture images) and we extend the methodology to the extraction of 3D shapes. In particular we test our algorithm on 2D and 3D ultrasound images in which the signal to noise ratio is truly small and the most part of the edge is missing.

The paper is organized as the following. In Section 2 we review past work in segmentation of images with missing boundaries. In Section 3 we discuss the mathematical problem and in Section 4 we present a numerical method to solve it. In Section 5 the extension of the 2D subjective surface

model to 3D manifolds is presented. In Section 6, we show results of the application of the method to different 2D images and discuss both the modal and amodal completion scenarios. In Section 7, results of the application of subjective manifolds to 3D image completion are presented and a validation of the method on 3D echocardiographic images is provided. In Section 8, a discussion about the accuracy and the efficiency of the computational model is also provided.

2   Past Work and Background

In this section, we review some previous work aimed at recovering subjective contours. We are interested in recovering explicit shape representations that reproduce that of the human visual perception, especially in regions with no image-based constraints such as gradient jump or variation in texture. In Mumford [26], the distribution of subjective contours are modeled and computed by particles traveling at constant speeds but moving in directions given by Brownian motion. Williams and Jacobs [41, 42] introduce the notion of a stochastic completion field, the distribution of particle trajectories joining pairs of position and direction constraints, and show how it could be computed. In this approach, a distribution of particles is being computed, rather than an explicit contour/surface, closed or otherwise.

A combinatorial approach is considered in [36]. A sparse graph is constructed whose nodes are salient visual events such as contrast edges and L-type and T-type junctions of contrast edges, and whose arcs are coincidence and geometric configurational relations among node elements. An interpretation of the scene consists of choices among a small set of labels for graph elements. Any given labeling induces an energy, or cost, associated with physical consistency and figural interpretation.

A common feature of both completion fields, combinatorial methods, as well as variational segmentation methods [25] is to postulate that the segmentation process is independent of observer's point of focus. On the other hand, methods based on active contours perform a segmentation strongly dependent on the user/observer interaction. Since their introduction in [13], deformable models have been extensively used to integrate boundaries and extract features from images. An implicit shape modeling approach with topological adaptability and significant computational advantages has been introduced in [21, 1, 22]. In these papers, the level set approach [28, 39] is used

to frame curve motion with a curvature-dependent speed. These and a host of other related works rely on edge information to construct a shape representation of an object. In the presence of large gaps and missing edge data, the models can go astray and away from the required shape boundary. This behavior is due to a constant speed component in the governing equation that helps the curve from getting trapped by isolated spurious edges. On the other hand, if the constant inflation term is switched off, as in [2, 33], the curve has to be initialized close to the final shape for reasonable results. We also note a more recent segmentation approach introduced in [4], in which the authors use geometric curve evolution for segmenting shapes without gradient by imposing a homogeneity constraint. An exhaustive review of algorithms for grouping is outside the purpose of this paper; we refer the interested reader to [19] for a larger perspective as well as for the classification of grouping algorithms in the broad families of region-based and contour-based approaches.

The approach in this paper rests on view that segmentation, regardless of dimensionality, is a 'view-point' dependent computation[1]. The "view-point" or the user-defined initial guess to the segmentation algorithm serves as input to the algorithm, and is used to construct a point-of-view surface. Next, this reference surface is evolved according to a feature-indicator function. The shape completion aspect relies on two components: (1) the evolution of a surface and (2) a flow that combines the effects of level set curve evolution with that of surface evolution. In what follows, we present a geometric framework that makes this possible. Computing the final segmentation (a contour or surface) is accomplished by choosing and plotting a particular level set of a higher dimensional function; as we shall show, this particular level set may be chosen automatically.

3 Theory

3.1 Local feature detection

Consider an image $\mathcal{I} : (x, y) \rightarrow I(x, y)$ as a real positive function defined in some domain $M \subset R^2$. One initial task in image understanding is to build a representation of the local structure of the image. This often involves detection of intensity changes, orientation of structures, T-junctions and texture. The result of this stage is a representation corresponding to *the raw primal sketch* [24]. Several methods have been proposed to compute the raw primal sketch, including

---

[1]It should be noted that this view of segmentation is in itself 'view-point' dependent.

multiscale/multiorientation image decomposition with Gabor filtering [6], wavelet transform [16], deformable filter banks [30], textons [15, 20] etc. For the purpose of the present paper we consider a simple edge indicator, namely

$$g(x,y) = \frac{1}{1 + (|\nabla G_\sigma(x,y) \star I(x,y)|/\beta)^2} \qquad \text{where} \qquad G_\sigma(\xi) = \frac{\exp(-(\xi/\sigma)^2)}{\sigma\sqrt{\pi}} \qquad (1)$$

The edge indicator function $g(x,y)$ is a non-increasing function of $|\nabla G_\sigma(x,y) \star I(x,y)|$, where $G_\sigma(x,y)$ is a Gaussian kernel and $(\star)$ denotes the convolution. The denominator is the gradient magnitude of a smoothed version of the initial image. Thus, the value of g is closer to 1 in flat areas ($|\nabla I| \to 0$) and closer to 0 in areas with large changes in image intensity, i.e. the local edge features. The minimal size of the details that are detected is related to the size of the kernel, which acts like a scale parameter. By viewing g as a potential function, we note that its minima denotes the position of edges. Also, the gradient of this potential function is a force field that always points in the local edge direction; see Figure 2.
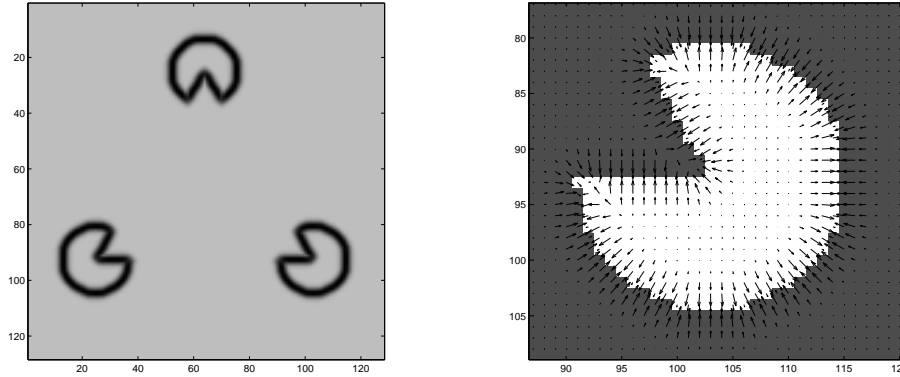

Figure 2: Local edge detection: The edge map g and its spatial gradient $-\nabla g$.

To compute $\nabla G_\sigma(x,y) \star I(x,y)$, we use the convolution derivative property $\nabla G_\sigma(x,y) \star I(x,y) = \nabla(G_\sigma(x,y) \star I(x,y))$ and perform the convolution by solving the linear heat equation

$$\frac{\partial \varphi}{\partial t} = \nabla.(\nabla \varphi) \qquad (2)$$

in the time interval $[0,\sigma]$ with the initial condition $\varphi(x,y,0) = I(x,y)$. We conclude this subsection by observing that there are other ways of both smoothing an image as well as computing an edge

indicator function or in general a feature indicator function, see, for example, [2, 22, 18, 29, 32, 40, 14].

3.2   Global boundary integration

Now, consider a surface $S : (x, y) \longrightarrow (x, y, \Phi)$ defined in the same domain M of the image I. The differential area of the graph S in the Euclidean space is given by:

$$dA = \sqrt{1 + \Phi_x^2 + \Phi_y^2} \; dx \; dy \tag{3}$$

We will use the edge indicator g to stretch and shrink a metric appropriately chosen so that the edges act as attractors under a particular flow. With the metric g applied to the space, we have

$$dA_g = g(x, y)\sqrt{1 + \Phi_x^2 + \Phi_y^2} \; dx \; dy. \tag{4}$$

Now, consider the area of the surface

$$A_g = \int_M g(x, y)\sqrt{1 + \Phi_x^2 + \Phi_y^2} \; dx \; dy, \tag{5}$$

(see Appendix A for derivation) and evolve the surface in order to reduce it. The steepest descent of Eqn. 5 is obtained with usual multivariate calculus techniques and results in the following flow

$$\frac{\partial \Phi}{\partial t} = g\frac{(1 + \Phi_x^2)\Phi_{yy} - 2\Phi_x\Phi_y\Phi_{xy} + (1 + \Phi_y^2)\Phi_{xx}}{1 + \Phi_x^2 + \Phi_y^2} + (g_x\Phi_x + g_y\Phi_y) \tag{6}$$

(see Appendix B for derivation)[2]. The first term on the right hand side is a parabolic term that evolves the surface in the normal direction under its mean curvature weighted by the edge indicator g. The surface motion is slowed down in the vicinity of edges (that is, where $g \rightarrow 0$). The second term on the right corresponds to pure passive advection of the surface along the underlying velocity field $-\nabla g$ whose direction and strength depend on position. This term pushes/attracts the surface in the direction of the image edges. Note that $g(I(x, y))$ is not a function of the third coordinate, therefore the vector field $-\nabla g$ lies entirely on the (x, y) plane.

The following characterizes the behavior of the flow (Eqn. 6):

---

[2] Note that this is the mean curvature flow in a Riemannian space with conformal metric $g\delta_{ij}$.

1. In regions of the image where edge information exists, the edge indicator $g \to 0$ and the main equation (Eqn. 6) reduces to a simple advection equation:

$$\frac{\partial \Phi}{\partial t} \approx g_x \Phi_x + g_y \Phi_y \qquad (7)$$

   driving the surface towards the edges. The level sets of the surface are attracted to the edge and accumulate. Consequently, the spatial gradient increases and the surface begins to develop a discontinuity.

2. Inside homogeneous regions of the image the edge indicator $g = 1$, and Eqn. 6 reduces to the Euclidean mean curvature flow:

$$\frac{\partial \Phi}{\partial t} = \frac{(1 + \Phi_x^2)\Phi_{yy} - 2\Phi_x \Phi_y \Phi_{xy} + (1 + \Phi_y^2)\Phi_{xx}}{1 + \Phi_x^2 + \Phi_y^2} \qquad (8)$$

   whose solutions are the horizontal planes characterizing the inside of the figures and the background.

3. We now address the regions in the image corresponding to subjective contours. We take the view that appropriate subjective contours are continuation of existing edge fragments. As discussed above, in regions with well defined edge information, Eqn. 6 causes the level curves to accumulate, thereby causing an increase in the spatial gradient of Φ. Since continuity for the surface is required during the evolution, the edge fragment information is propagated to complete the missing boundary. When spatial derivatives $\Phi_x, \Phi_y \gg 1$, Eqn. 6 is approximated by

$$\frac{\partial \Phi}{\partial t} \approx g \frac{\Phi_x^2 \Phi_{yy} - 2\Phi_x \Phi_y \Phi_{xy} + \Phi_y^2 \Phi_{xx}}{\Phi_x^2 + \Phi_y^2} + (g_x \Phi_x + g_y \Phi_y). \qquad (9)$$

   which is commonly known as the geodesic level set flow [2, 23]. This flow moves the level curves of the surface towards geodesic curves; which are curves of minimal path length connecting existing boundaries. Subjective contours are then straight lines connecting the local features.

4. In regions where $\Phi_x, \Phi_y \ll 1$ Eqn. 6 may be approximated by

$$\frac{\partial \Phi}{\partial t} \approx g(\Phi_{xx} + \Phi_{yy}) + (g_x \Phi_x + g_y \Phi_y). \qquad (10)$$

9

This is a non-uniform diffusion equation and describes the steepest descent of the weighted $L2$ norm, namely

$$\int g|\nabla\Phi|^2 \, dxdy. \tag{11}$$

If the image gradient inside the object is actually equal to zero, then $g = 1$, Eqn. 10 becomes a simple linear heat equation, and the flow corresponds to linear uniform diffusion.

The main equation (Eqn. 6) is a mixture of two different dynamics, the level set flow (Eqn. 9) and pure diffusion (Eqn. 10). Locally, points on the Φ surface move according to one of these mechanisms [31]. In steady state solution, the points inside the objects are characterized by pure linear diffusion, while points on the boundary are characterized by the geodesic level set flow. The scaling of the function Φ weights the two dynamics. If Φ contains a narrow range of values, the derivatives are small and the behavior of the flow (6) is mostly diffusive. Conversely, where Φ is contains large variation in values, the behavior mostly consists of level set plane curve evolution. We perform the scaling by multiplying the initial surface (x, y, Φ_0) (point of view surface) with a scaling factor α.

Remark 1. In the most general case the metric of a Riemannian space is a tensor h_{ij}. In Appendix A we derive the area of a surface embedded in such a manifold. In this paper, we have considered a simple conformal metric $h_{ij} = g\delta_{ij}$ which contains only scalar information about the local image boundaries. In the general case, the tensor metric can be constructed in such a way to contain more information about the local structure of the image like edge direction, color and texture.

Remark 2. In [25], Mumford and Shah perform image segmentation by analyzing the energy functional:

$$E(\Phi, \Gamma) = \lambda^2 \int_{\Omega-\Gamma} |\nabla\Phi|^2 \, dxdy + \mu^2 \int_{\Gamma} d\sigma + \int_{\Omega-\Gamma} (\Phi - I)^2 \, dxdy \tag{12}$$

where Ω is the image domain and Γ is the set of piece-wise smooth boundaries of the objects contained in the image. They look for a minimization of E, that is the smaller E is, the better (Φ, Γ) segments I:

- The first term tries to flatten Φ inside the objects, that is in the domain $\Omega - \Gamma$.

10

- The second term tries to minimize the length of the boundaries Γ.

- The third term drives Φ to approximate I.

We now consider the relationship between a subjective surface and the minimization of Eqn. 12.

- Inside the objects, the subjective surface is flat (driven by the linear diffusion flow), so that the first integral in (12) is identically zero.

- The boundaries of the subjective surface are "geodesic" curves, in fact, they are driven by the level set geodesic flow, as pointed earlier. They link the existing feature points present in the image using paths of minimal length. The boundary Γ of the subjective surface minimizes the second integral in (12)

- Most importantly, the subjective surface is an approximation of the point-of-view surface and not of the image I, as controlled by the third integral in (12). We first point out that the third constraint can be matched by initializing $\Phi_0 = I$ in the flow given in Eqn. 6. Notice that by doing so, the segmentation process cannot segment objects with the same intensity of the background; ruling out the Kanitza triangle and most of the images with subjective contours. In contrast, by initializing with the point-of-view surface, we force the object initialized by the fixing point to evolve *independent of the gray level in the image*.

4 Numerical Scheme and Computational Model

In this section, we show how to approximate Eqn. 6 with finite differences. We consider a rectangular uniform grid in space-time (t, x, y); then the grid consists of the points $(t_n, x_i, y_j) = (n\Delta t, i\Delta x, j\Delta y)$. Following standard notation, we denote by Φ_{ij}^n the value of the function Φ at the grid point (t_n, x_i, y_j). We approximate time derivative with a first order forward difference. The first term of Eqn. 6 is a parabolic contribution to the equation of motion and we approximate this term with central differences. The second term on the right corresponds to passive advection along an underlying velocity field ∇g whose direction and strength depend on edge position; this term is approximated using upwind schemes, which are used to approximated spatial derivative in a way which respects the appropriate entropy condition for propagating fronts [37, 38]. In order

11

to build a correct entropy-satisfying approximation of the difference operator, we exploit the technology of hyperbolic conservation laws. In other words, we check the sign of each component of ∇g and construct one-sided difference approximation to the gradient in the appropriate (upwind) direction; for details of upwind schemes applied to these equations, see [28].

With this, we can write a complete scheme to approximate Eqn. (6) as follows:

$$\Phi_{ij}^{n+1} = \Phi_{ij}^n + \Delta t \left\{ \begin{array}{l} \left[g_{ij} \dfrac{(1+D_{ij}^{0x^2})D_{ij}^{0yy} - 2D_{ij}^{0x}D_{ij}^{0y}D_{ij}^{0xy} + (1+D_{ij}^{0y^2})D_{ij}^{0xx}}{1+D_{ij}^{0x^2}+D_{ij}^{0y^2}} \right] \\ - \left[\begin{array}{l} [\max(g_{ij}^{0x},0)D_{ij}^{-x} + \min(g_{ij}^{0x},0)D_{ij}^{+x} \\ + \max(g_{ij}^{0y},0)D_{ij}^{-y} + \min(g_{ij}^{0y},0)D_{ij}^{+y}] \end{array} \right] \end{array} \right\} \tag{13}$$

where D is a finite difference operator on Φ_{ij}^n, the superscripts $\{-, 0, +\}$ indicate backward, central and forward differences respectively, and the superscripts $\{x, y\}$ indicate the direction of differentiation. We impose Dirichlet boundary conditions by fixing the value on the boundary equal to the minimum value of the point-of-view surface. The time step Δt is upper bounded by the CFL (Courant-Friedrich-Levy) condition that insures the stability of the evolution [17].

We summarize the computational steps below:

Segmentation and modal completion of an object with missing boundaries

- First, given an image I, chose a point inside the object (fixation point). Next, build the point-of-view surface Φ_0 by computing the distance function from the fixation point (alternate choice is given in Section 6).

- Compute the edge indicator function g (see Eqn. 1) corresponding to the given image I.

- Evolve the point-of-view surface towards a piecewise constant solution (subjective surface) according to Eqn. 13.

- Find the boundary of the segmented object by picking the level set: $\bar{\Phi} = \{\max(\Phi) - \epsilon\}$, for a small $\epsilon > 0$.

Note: Given the edge map g, the only interactive part in the above algorithm is the fixation point choice.

Amodal completion of a partially occluded object

- First, segment the occluding object O_1.

- Build a new edge map $g_{new} = \begin{cases} 1 & (x, y) \in O_1 \\ g & otherwise \end{cases}$

- Use g_{new} to perform modal completion of the partially occluded object

Note: Again, given the edge map g, the only interaction required is the original fixation point choice.

5   3D Subjective Manifolds

In this section we extend the subjective surfaces methodology to the extraction of shapes from volumetric images. Consider a volumetric image $\mathcal{I} : (x, y, z) \to I(x, y, z)$ defined in $M \subset R^3$. As in the 2D case we define a simple edge indicator acting on I

$$g(x, y, z) = \frac{1}{1 + (|\nabla G_\sigma(x, y, z) \star I(x, y, z)|/\beta)^2} \qquad \text{where} \qquad G_\sigma(\xi) = \frac{\exp(-(\xi/\sigma)^2)}{\sigma\sqrt{\pi}}. \quad (14)$$

We now consider a 3D manifold $V = (x, y, z) \longrightarrow (x, y, z, \Phi(x, y, z))$ defined on the same domain of $\mathcal{I}$. The 3D manifold is embedded in a 4-D Riemannian space with conformal metric $h_v = g(x, y, z)\delta_{ij}$. Analogous to surface area in the 2D case, we define the volume of the manifold as:

$$V_g = \int_\Omega g\sqrt{1 + \Phi_x^2 + \Phi_y^2 + \Phi_z^2}\, dx\, dy\, dz. \quad (15)$$

See Appendix A for derivation. The minimizing flow for the volume functional is then given by the steepest descent of (15), namely

$$\frac{\partial \Phi}{\partial t} = g \frac{(1+\Phi_x^2+\Phi_y^2)\Phi_{zz} + (1+\Phi_x^2+\Phi_z^2)\Phi_{yy} + (1+\Phi_z^2+\Phi_y^2)\Phi_{xx} - 2\Phi_x\Phi_z\Phi_{xz} - 2\Phi_x\Phi_y\Phi_{xy} - 2\Phi_y\Phi_z\Phi_{yz}}{1+\Phi_x^2+\Phi_y^2+\Phi_z^2} + \quad (16)$$

$$g_x\Phi_x + g_y\Phi_y + g_z\Phi_z$$

that is derived with usual multivariate calculus in Appendix B.

The numerical scheme used to approximate Eqn. 16 is almost identical to that for Eqn. 13; for completeness, we have

$$\phi_{ijk}^{n+1} = \phi_{ijk}^n + \Delta t \left[\begin{array}{l} g_{ijk}\left[\dfrac{(1+D_{ijk}^{0x^2}+D_{ijk}^{0y^2})D_{ijk}^{0zz} + (1+D_{ijk}^{0x^2}+D_{ijk}^{0z^2})D_{ijk}^{0yy} + (1+D_{ijk}^{0z^2}+D_{ijk}^{0y^2})D_{ijk}^{0xx}}{1+D_{ijk}^{0x^2}+D_{ijk}^{0y^2}+D_{ijk}^{0z^2}}\right. \\ \qquad\qquad \left. -2\dfrac{D_{ijk}^{0x}D_{ijk}^{0z}D_{ijk}^{0xz} + D_{ijk}^{0x}D_{ijk}^{0y}D_{ijk}^{0xy} + D_{ijk}^{0y}D_{ijk}^{0z}D_{ijk}^{0yz}}{1+D_{ijk}^{0x^2}+D_{ijk}^{0y^2}+D_{ijk}^{0z^2}}\right] \\ -\left\{\begin{array}{l} [\max(g_{ijk}^{0x},0)D_{ijk}^{-x} + \min(g_{ijk}^{0x},0)D_{ijk}^{+x} \\ + \max(g_{ijk}^{0y},0)D_{ijk}^{-y} + \min(g_{ijk}^{0y},0)D_{ijk}^{+y} \\ + \max(g_{ijk}^{0z},0)D_{ijk}^{-z} + \min(g_{ijk}^{0z},0)D_{ijk}^{+z}] \end{array}\right\} \end{array}\right] \quad (17)$$

where the same notation of Eqn. 13 has been adopted.

6   2D Image Completion

In this section, we present results of several computations aimed at performing both modal and amodal completion of objects with missing boundaries. The input to the algorithm is a user-defined

point-of-view or a reference surface and an edge indicator function computed as a function of the image. Different choices exist for the reference surface; as examples, we show two such choices in Fig. 3. In the next examples we use $\Phi_0 = \alpha/\mathcal{D}$, where $\mathcal{D}$ is the distance from the initial point of view and α is a scaling factor; $\alpha = 10^3$ is the fixed value that we use.

6.1 Synthetic Images

First, we consider the classical triangle of Kanizsa (Fig. 1) and apply the algorithm in order to perform a modal completion of the missing boundaries. We first compute the edge map as shown in the left image of Fig. 4, and then choose a reference point approximately at the center of the perceived triangle (center image of Fig. 4). The evolution of the surface under the flow induced by Eqn. 6 is visualized in Fig. 5. The computed subjective surface is the steady-state piece-wise linear surface shown at the end of this sequence. The triangle boundary shown in the right image of Fig. 4 is found by plotting the level set $\bar{\Phi} = \{\max(\Phi) - \epsilon\}$ of the subjective surface. Note that in visualizing the surface, we normalize it with respect to its maximum.
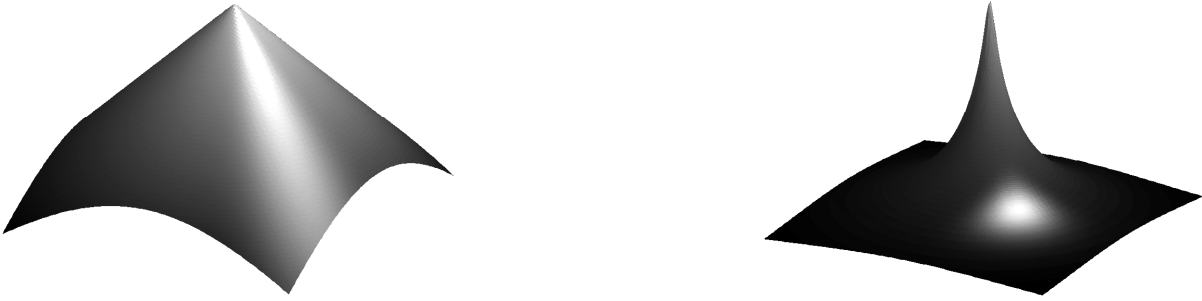
Figure 3: Point-of-view surfaces: on the left $\Phi_0 = -\alpha\mathcal{D}$, where $\mathcal{D}$ is the distance function from the fixation point, and on the right $\Phi_0 = \alpha/\mathcal{D}$.

15
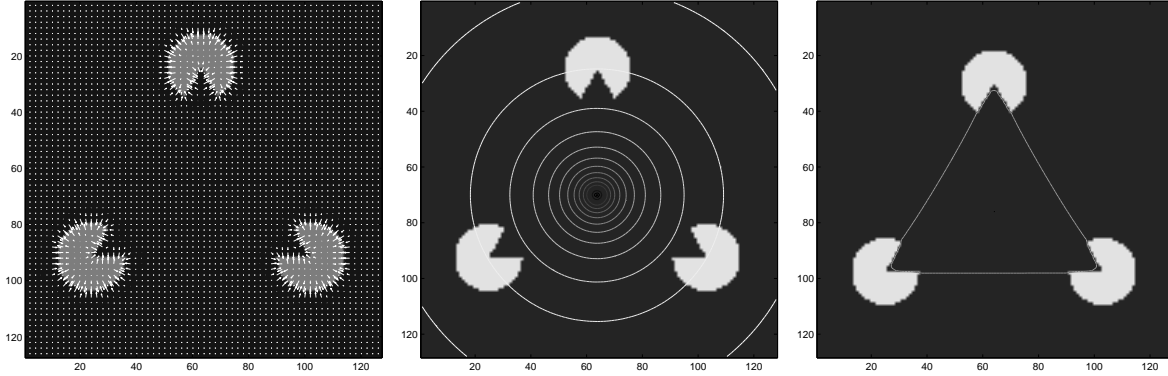
Figure 4: Three steps of the modal completion of the triangle of Kanizsa: on the left the edge indicator $-\nabla g(I)$ is shown, in the center a set of equi-spaced contour lines of the point-of-view surface are drawn, and on the right is the level set of the subjective surface that corresponds to the triangle boundary.
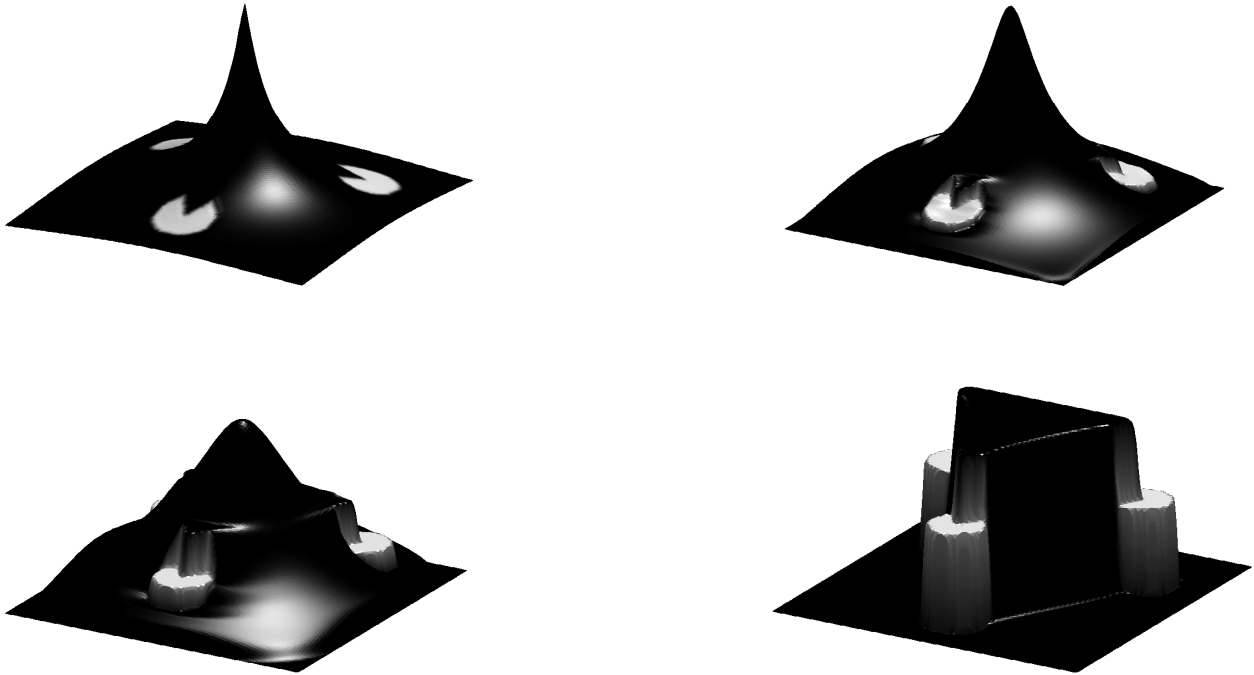

Figure 5: Four time frames showing the evolution of the point-of-view surface (upper left) towards the subjective surface (bottom right). In this visualization the original image has been texture mapped onto the surface.

In the previous section, we noted that our main equation (Eqn. 6) is a combination of two dynamics: a level set flow on one end and a linear diffusion at the other. In the next experiment, we show what the modal completion result looks like under these two extremes specially for the case when the user-defined fixation point is a bit off center. In the left image of Fig. 6, we consider a slightly off center initial condition. As shown in the right image of Fig. 6, the flow under Eqn. 6 succeeds in producing a good segmentation of the triangle. If we consider a strongly off center initial condition as in Fig. 7, the triangle is still present in the subjective surface, but the closest white inducer becomes predominant. On the other hand, the flows under both Eqn. 9 and Eqn. 10 fail to produce a good modal completion even with a slightly off center point of view; see Fig. 8. The level set flow (Eqn. 9) causes the formation of false surface gradient due to the off center initial condition (Fig. 8, left), and the flow under Eqn. 10 produces a result that is too diffusive (Fig. 8, right). The same parameters have been chosen for the all experiments.
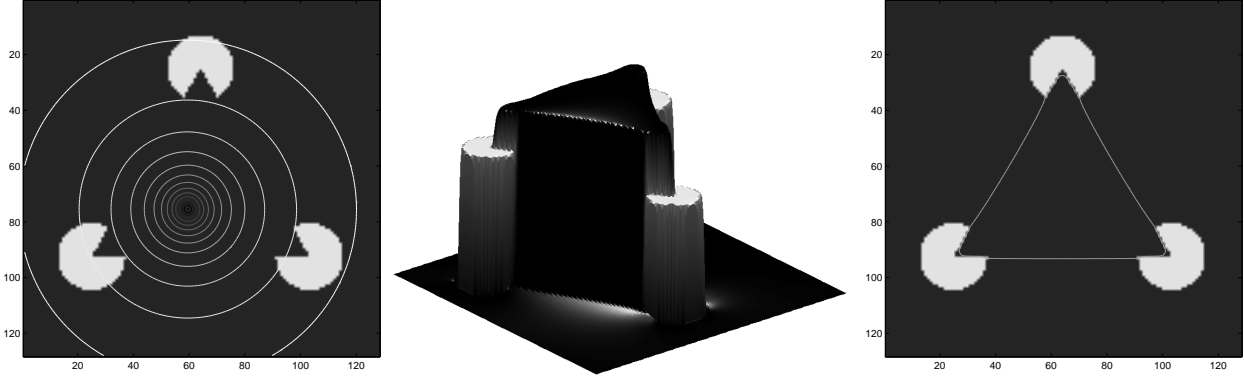
Figure 6: A slightly off center fixation point: on the left equispaced contour lines of the point-of-view surface are shown and the computed triangular contour is shown on the right.

Next, we present a series of results of computing subjective surfaces. In Fig. 9, we show the subjective surface computation from an image with little or no (aligned) edge information. We render the perceived square in the final image of Fig. 9. The parameters of the edge map are $\sigma = 0.3$ pixels and $\beta = 0.5$. As mentioned in the introductory section, the initial surface can be evolved using any "feature-indicator" and not just under the influence of an edge-indicator function g. In order to perform texture segmentation, we replace the usual edge-indicator $g(I)$ with the orientation detector $g(|J_v|)$, where J_v is the Jacobian of $\vec{v} = \frac{I_x^2 - I_y^2, 2I_xI_y}{I_x^2 + I_y^2}$. The result of this
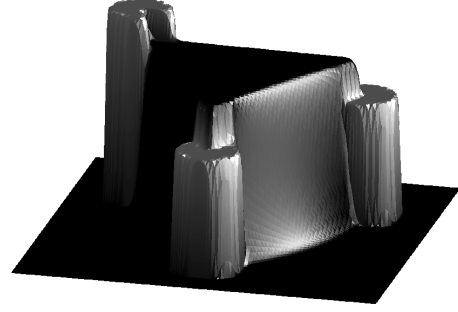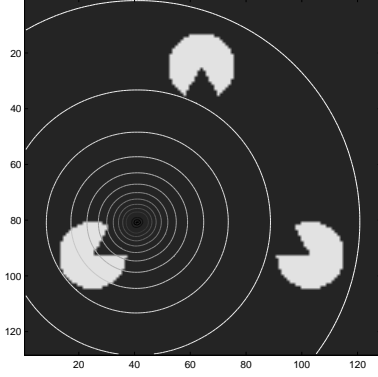
Figure 7: A strongly off center fixation point: on the left equispaced contour lines of the point-of-view surface are shown and on the right the subjective surface is visualized.
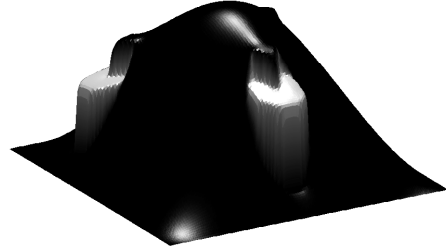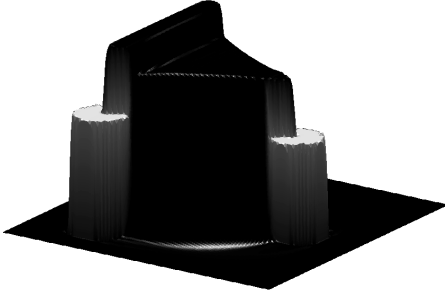

Figure 8: Comparison with different norms: On the left is shown the result of the segmentation with pure level set curve evolution (Equation (9)). On the right is shown the result of the segmentation with pure nonuniform diffusion (Equation (10)).The point of view surface is the same as in Fig.6).

computation is shown in Fig. 10. If an image consists of several objects connected with narrow necks, as in Fig. 11, more then one point of view has to be selected in order to segment the entire shape. This is in contrast to methods where the contour "flows" through these gaps from one initial seed point, see [22, 23].
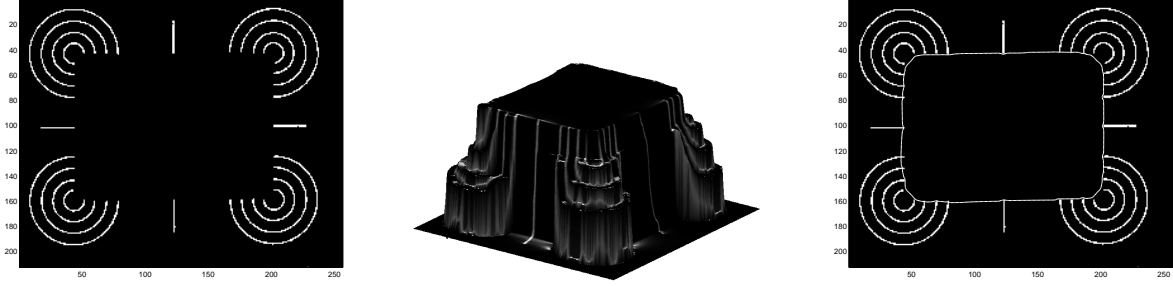
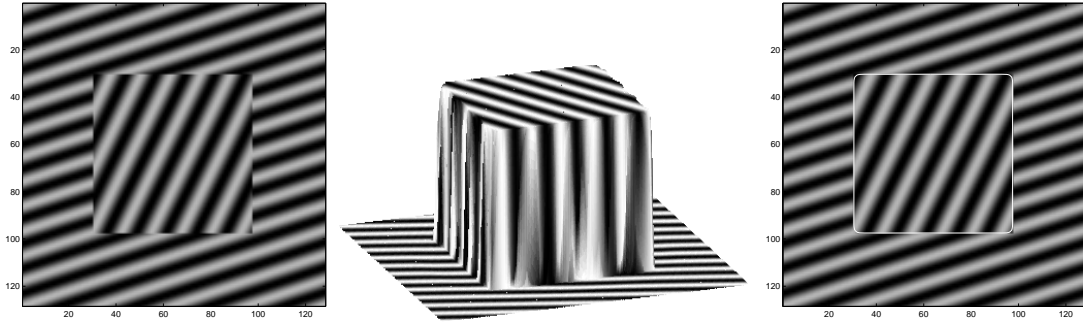Figure 9: Modal completion of an image without any aligned gradient.

Figure 10: Texture segmentation can be performed using a different feature-indicator function instead of the usual edge indicator function.
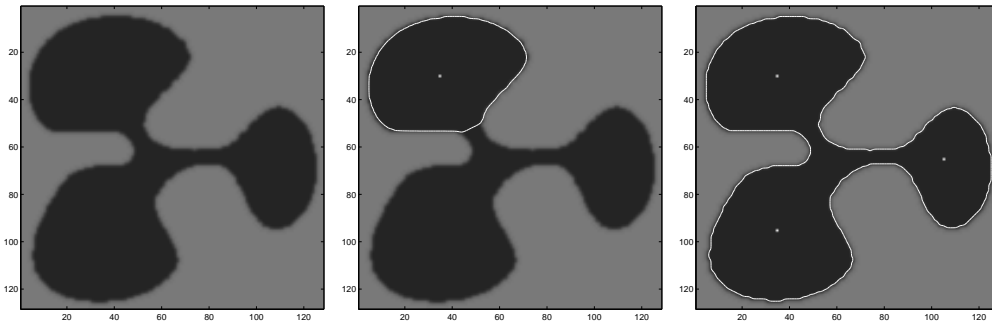

Figure 11: Segmentation of a figure containing several objects (left). If only one point of view is chosen (center), the corresponding object is segmented. To segment the entire shape, several point of views have to be selected (right).

19

The subjective contours we have considered so far are called "modal" contours because they are "perceived" in the visual experience. Now we consider "amodal" contours that are present in images with partially occluded shapes. Consider the example of a white square partially occluded by a gray disk as shown in Fig. 12. Our goal is to recover the shapes of both the square and the disk. We employ a three step procedure: first, we build the edge map g_1 ($\sigma = 0.3$ pixels and $\beta = 0.5$) of the image, choose a point of focus inside the disk and perform the segmentation of the grey disk O_{disk}. Second, we build another edge map $g_2 = \left\{ \begin{array}{ll} 1 & (x,y) \in O_{disk} \\ g_1 & otherwise \end{array} \right\}$, so that all the image features belonging to the first object are inhibited in the new function. As the third step we perform the modal completion of the partially occluded square using the new edge map g_2. Again, the process is completely automatic after the initial point of reference is chosen. The entire process is shown in Fig. 12.
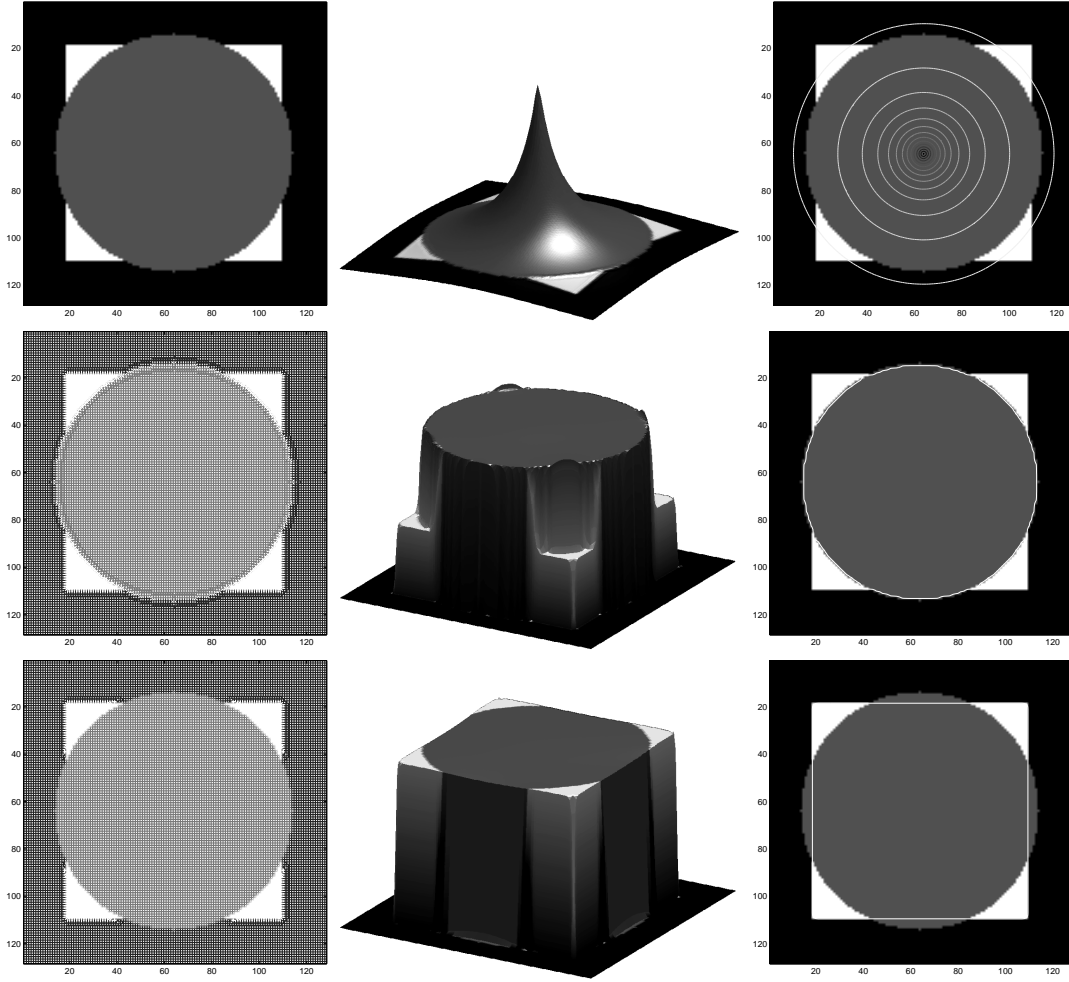
Figure 12: Amodal completion of the white square partially occluded by the gray disk. In the first row the original image (left) and the point-of-view surface (center, right) are shown. In the second row, the edge map g_1 (left), the subjective surface (center), and the occluding disk boundary (right) are shown. The amodal completion of the square is shown in the third row. The new edge map g_2 (left) is obtained from the previous one by simply removing the features corresponding to the occluding object (disk). This new edge map allows the formation of a new subjective contour (center) and the square boundary (right). We use the value $\beta = 0.3$ in the edge indicator.

6.2 Real Images

Echographic images are difficult candidates for shape recovery for two reasons. First, they possess highly noisy structures, and second, large parts of the boundary are often missing, making shape recovery difficult. One application of our algorithm is in segmenting boundaries with non-continuous edges in extremely noisy images. In Fig. 13, we show one such computation; we use a line initialization instead of a fixation point and the point-of-view surface is constructed to be the distance function from this initial line. The final result, a particular level set of the subjective surface is shown in the right image of Fig. 13. In Fig. 14, we show four stages of the subjective surface evolution, where natural boundary conditions have been imposed.

Next, in Fig. 15, we show the recovery of missing boundaries in four echographic images. We construct an edge indicator with $\beta = 0.1$ and $\sigma = 1.0$ and follow exactly the same procedure to recover all the four shapes of interest.

Figure 13: Segmentation of fetal echogram: modal completion is needed to recover a large portion of the missing boundary in the dorsal section of the fetus. The original image (left), the line of view (center) and the segmented boundary (right) are shown.

Finally, we present a set of amodal completion results from a photograph. As shown in Fig. 16 our test image is one of a trash can placed in front of a computer monitor and our goal is to extract the outline of the computer monitor that is partially occluded by the trash can. In the first row of Fig. 16 (left to right), we show the original image, the point-of-view surface, and some of its level curves. The initial point of reference is chosen to be inside the trash can region. The first step is to extract the shape of the trash can using the original edge map information ($\beta = 0.1, \sigma = 0.3$ pixels);
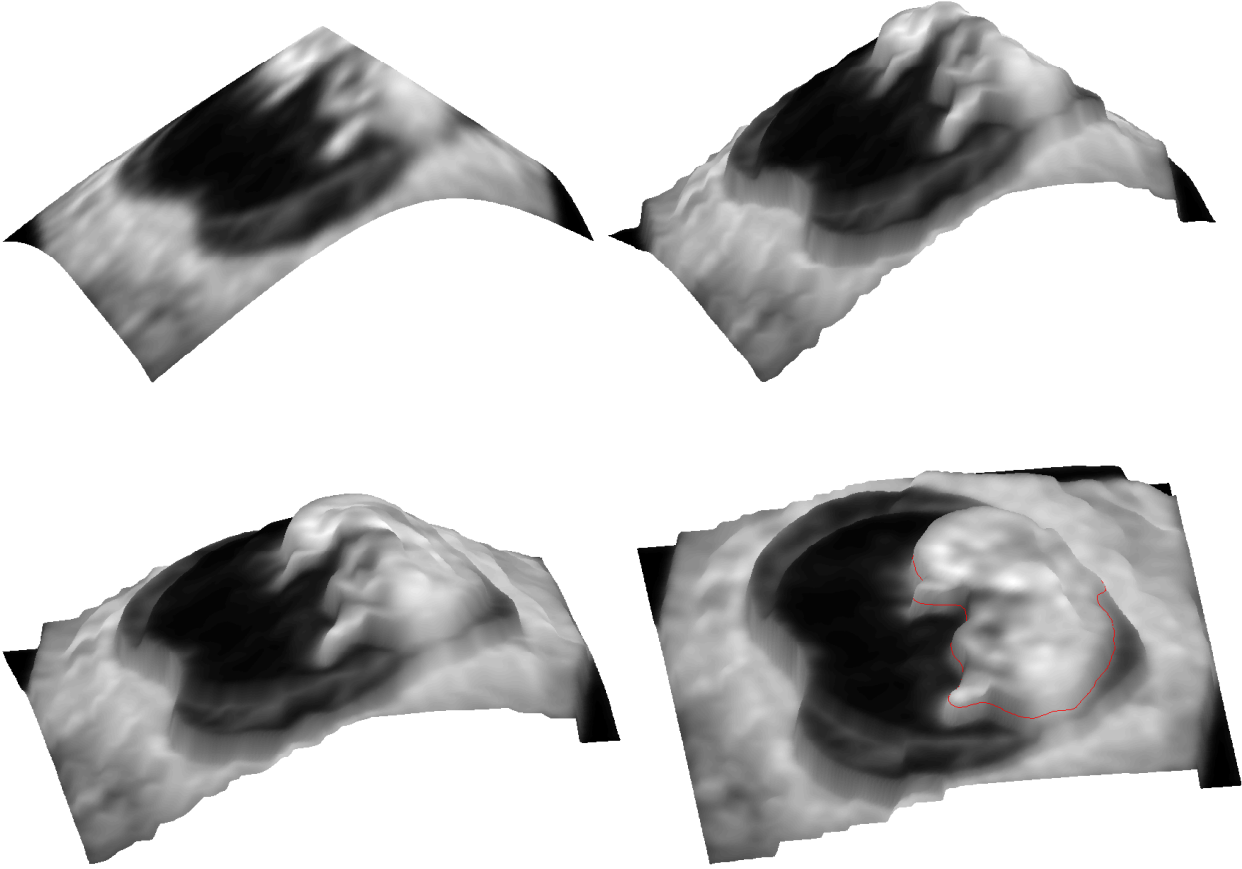
Figure 14: Four time frames depicting the minimization process that flows the initial surface (upper left) towards the subjective surface (bottom right)

this step is shown in the second row of the figure. Once the trash can shape has been extracted, its edge features are eliminated to produce a new edge indicator function shown in the left image of the third row of Fig. 16. Under the influence of this edge function, we succeed in extracting the shape of partially occluded computer screen; see the third row of the figure. We then repeat the process and eliminate the edge features corresponding to the computer screen, producing yet another edge function. The flow (Eqn. 6) under the edge function shown in the left image of the bottom row produces the subjective surface (bottom center) and the shape of the partially occluded computer monitor (bottom right).

7   3D Image Completion

Next, we present a series of results of computing subjective manifolds to extract 3D shapes. We apply the segmentation model/algorithm to an *in vivo* acquired 3D echocardiographic sequence. The sequence has been obtained by means of a rotational acquisition technique using the TomTec Imaging System. With this technique, the transducer undergoes a rotation around its main axis in a propeller configuration. A series of tomographies corresponding to the sections of a cone of biological tissue has been acquired. The acquisition consists of 14 image-cubes that represent an entire cardiac cycle of a patient, and a volume of interest of 150 x 150 x 100 voxels is processed. The interval of time between one cube and the next one is 40 ms. In figure 7, the extracted ventricular chamber in 4 different time frames of the cardiac cycle is shown; the time interval is 120 ms. In order to evaluate the accuracy of the 3D segmentation, we follow the procedure presented in [32]. An external observer has manually segmented the ventricular chamber by considering every single slice l of a 3D frame. We consider this manual segmentation as our Gold Standard; we now compute the distance between the Gold Standard and the automatic extracted shape. For each slice a distance function $\mathcal{D}_l(x,y)$ from the automatic segmented surface is computed. The mean distance between the manual segmentation curve C_l and the extracted shape is defined as $D_l = \int_{C_l} \mathcal{D}_l(x,y)ds / \int_{C_l} ds$, where s is the arclenght. The distance error has been evaluated for every slice of the 3D data set. The global distance error is computed by averaging the errors over the L slices, i.e. $D = \frac{1}{L}\sum_{l=1}^{L} D_l$. With this procedure we estimated $D = 0.9$ voxels. See [32] for further details.

Finally, we computed a subjective manifold for 3D fetal echography. The reference line is the same as in Fig. 13 and a 3D distance function from it has been computed and used as initial manifold. The resulting segmentation of the fetus is visualized in Fig 7.

8   Accuracy and Efficiency

Next, we address the evaluation of the accuracy of the proposed method. We distinguish between the accuracy in detecting existing boundaries (in which the edge indicator g is active) and the accuracy of determining subjective contours. In the case of real boundaries, the position of the contour line is indicated by the vector field $-\nabla g$ which is the gradient of the edge indicator. The

contour line is then regularized with the parabolic term of Eqn. 6, that in these regions degenerates in Eqn. 9. We rely on an extensive validation and accuracy estimation for the flow (Eqn. 9) that has been discussed in [34]. It is more problematic to evaluate accuracy in detecting subjective contours. Our method reduces to the geodesic active contour model near the edges and therefore finds shortest possible edge extensions when completing missing information. In contrast, we note that the visual system is able to recover curved subjective contours [10], by exploiting both position and direction of existing boundaries. A higher order subjective surface model is under investigation to provide curved subjective contours [35].

The computational complexity of the algorithm is of order $NP \times NI$ where NP is the number of pixels (voxels) of the 2D (3D) image and NI is the number of iterations required to solve Eqn. 13 (Eqn. 17). For an image of $N \times N$ pixels the number of iterations is about $4N$ and the computational time is the usual one required in solving a finite difference equation with explicit methods. The number of iterations scales for 3D images.

9   Appendix A

In this section we derive the area functional of a surface embedded in a 3D Riemannian space (Eqn. 5) and the volume functional of a 3D manifold embedded in a 4D Riemannian space (Eqn. 15). Let u, v be non-zero, non-parallel vectors in R^3. We note that

$$\|u\|^2\|v\|^2 - (u \cdot v)^2 = det\left((u,v)^T(u,v)\right) \tag{18}$$

where (u, v) is the matrix with column vectors u, v, and the area of the parallelogram is given by

$$A_p = \sqrt{det\left((u,v)^T(u,v)\right)}. \tag{19}$$

We apply this to a surface given by the graph of a function

$$z = \Phi(x, y), \tag{20}$$

defined over some region Ω of the (x, y)-plane so that

$$S(x, y) = (x, y, \Phi). \tag{21}$$

25

Then the two tangent vectors

$$\frac{\partial S}{\partial x} = (1, 0, \Phi_x)^T \quad and \quad \frac{\partial S}{\partial y} = (0, 1, \Phi_y)^T \tag{22}$$

span a parallelogram with area

$$f = \sqrt{det(J^T J)} = \sqrt{1 + \Phi_x^2 + \Phi_y^2} \tag{23}$$

where

$$J = \left(\frac{\partial S}{\partial x}, \frac{\partial S}{\partial y}\right) = \begin{pmatrix} 1 & 0 \\ 0 & 1 \\ \Phi_x & \Phi_y \end{pmatrix} \tag{24}$$

and the matrix

$$J^T J = \begin{pmatrix} 1 + \Phi_x^2 & \Phi_x \Phi_y \\ \Phi_x \Phi_y & 1 + \Phi_y^2 \end{pmatrix} \tag{25}$$

is the induced metric. The function f is called area density of S. The area of the surface is given by integrating the area density over the domain Ω

$$A = \int_\Omega \sqrt{1 + \Phi_x^2 + \Phi_y^2} \, dx \, dy. \tag{26}$$

We now consider a 3D Riemannian space (N, h) with metric

$$h = \begin{pmatrix} h_{11} & h_{12} & h_{13} \\ h_{12} & h_{22} & h_{23} \\ h_{13} & h_{23} & h_{33} \end{pmatrix} \tag{27}$$

that defines an inner product $< u, v > = u^T h v$, where $u, v \in N$. Then the area of the parallelogram spanned by u and v in (N,h) is given by

$$A_{ph} = \sqrt{det((u, v)^T h \ (u, v))} \tag{28}$$

Consequently the area density of a surface embedded in (N,h) is

$$f_h = \sqrt{det(J^T h J)} = \quad [(h_{11} h_{22} - h_{12}^2) + 2(h_{13} h_{22} - h_{12} h_{23})\Phi_x + 2(h_{11} h_{23} - h_{12} h13)\Phi_y + \tag{29}$$
$$(h_{22} h_{33} - h_{23}^2)\Phi_x^2 + 2(h_{13} h_{23} - h_{12} h_{33})\Phi_x \Phi_y + (h_{11} h_{33} - h_{13}^2)\Phi_y^2]^{1/2}$$

where

$$J^T h J = \begin{pmatrix} h_{11} + 2h_{13}\Phi_x + h_{33}\Phi_x^2 & h_{12} + h_{23}\Phi_x + h_{13}\Phi_y + h_{33}\Phi_x \Phi_y \\ h_{12} + h_{23}\Phi_x + h_{13}\Phi_y + h_{33}\Phi_x \Phi_y & h_{22} + 2h_{23}\Phi_y + h_{33}\Phi_y^2 \end{pmatrix} \tag{30}$$

is the induced metric. In the particular case in which the metric is conformal $h = g\delta_{ij}$, the area density simplifies

$$f_g = g\sqrt{det(J^T J)} \tag{31}$$

and the surface area becomes

$$A_g = \int_\Omega g\sqrt{1 + \Phi_x^2 + \Phi_y^2}\ dx\ dy.$$

that corresponds to Eqn. 5.

We now consider a 3-D manifolds $V = (x, y, z, \Phi)$ embedded in a 4-D Riemannian space with metric h_v. Similarly to the 2D case we define a volume density:

$$f_v = \sqrt{det(J_v^T h_v J_v)} \tag{32}$$

where

$$J_v = \left(\frac{\partial V}{\partial x}, \frac{\partial V}{\partial y}, \frac{\partial V}{\partial z}\right) = \begin{pmatrix} 1 & 0 & 0 \\ 0 & 1 & 0 \\ 0 & 0 & 1 \\ \Phi_x & \Phi_y & \Phi_z \end{pmatrix} \tag{33}$$

In the particular case in which the metric is conformal $h = g\delta_{ij}$, the volume density simplifies

$$f_{vg} = g\sqrt{det(J_v^T J_v)} \tag{34}$$

and the volume becomes

$$V_g = \int_\Omega g\sqrt{1 + \Phi_x^2 + \Phi_y^2 + \Phi_z^2}\ dx\ dy\ dz.$$

that is namely Eqn. 15.

10 Appendix B

In this section we derive the main flows (Eqn. 6) and (Eqn. 16). Consider the area functional (Eqn. 5) and look for its local minimum. Since critical points of a differentiable function are characterized by the vanishing of its differential, we consider the first variational formula of the functional

$$\tilde{H} \doteq \frac{\partial f_g}{\partial \Phi} - \frac{\partial}{\partial x}\frac{\partial f_g}{\partial \Phi_x} - \frac{\partial}{\partial y}\frac{\partial f_g}{\partial \Phi_y}. \tag{35}$$

The Euler-Lagrange equation

$$\tilde{H} = 0 \tag{36}$$

gives the condition of extremality [7] and it is by definition the equation of a minimal surface in the Riemannian space with metric $g\delta_{ij}$. By considering $g = g(I(x,y)) = g(x,y)$ and by applying usual multivariate calculus techniques to (Eqn. 35) we obtain

$$\tilde{H} = g\frac{(1 + \Phi_x^2)\Phi_{yy} - 2\Phi_x\Phi_y\Phi_{xy} + (1 + \Phi_y^2)\Phi_{xx}}{(1 + \Phi_x^2 + \Phi_y^2)^{3/2}} + \frac{(g_x\Phi_x + g_y\Phi_y)}{(1 + \Phi_x^2 + \Phi_y^2)^{1/2}} \tag{37}$$

that is the mean curvature of the submanifold $S = (x, y, \Phi)$ in the Riemannian space with conformal metric $g\delta_{ij}$ [27]. Starting from a surface $S_0 = (x, y, \Phi_0)$, the fastest way to achieve the condition (Eqn. 36) is the steepest descent of

$$\frac{\partial S}{\partial t} = \tilde{H}\ \tilde{\mathcal{N}} \tag{38}$$

where $\tilde{\mathcal{N}}$ is the inner normal of S in the Riemannian space. Since $\frac{\partial S}{\partial t} = \frac{\partial}{\partial t}(x, y, \Phi(x,y)) = (0, 0, \frac{\partial \Phi}{\partial t})$, the only non-null flow is in the direction $\vec{\Phi} = (0, 0, 1)$. As in [40], we rewrite Eqn. 38 in the direction $\vec{\Phi}$ as

$$\frac{\partial \Phi}{\partial t} = \tilde{H}\frac{1}{(\tilde{\mathcal{N}} \cdot \vec{\Phi})} \tag{39}$$

Since $\vec{\mathcal{N}} = \frac{(-\Phi_x, -\Phi_y, 1)^T}{\sqrt{1 + \Phi_x^2 + \Phi_y^2}}$ then:

$$\frac{1}{(\vec{\mathcal{N}} \cdot \vec{\Phi})} = \sqrt{1 + \Phi_x^2 + \Phi_y^2} \tag{40}$$

and by substituting Eqn. 37 and Eqn. 40 in Eqn. 39 we obtain:

$$\frac{\partial \Phi}{\partial t} = g\frac{(1 + \Phi_x^2)\Phi_{yy} - 2\Phi_x\Phi_y\Phi_{xy} + (1 + \Phi_y^2)\Phi_{xx}}{(1 + \Phi_x^2 + \Phi_y^2)} + (g_x\Phi_x + g_y\Phi_y)$$

which is the main flow (Eqn. 6) for 2D shapes extraction. When the embedding is Euclidean then $g = 1$ and we obtain the well known mean curvature flow:

$$\frac{\partial \Phi}{\partial t} = \frac{(1 + \Phi_x^2)\Phi_{yy} - 2\Phi_x\Phi_y\Phi_{xy} + (1 + \Phi_y^2)\Phi_{xx}}{(1 + \Phi_x^2 + \Phi_y^2)}. \tag{41}$$

Similarly we derive the flow for a 3-D manifolds embedded in a 4-D Riemannian space. Consider the volume functional 15. By applying the first variational formula

$$\tilde{H} \doteq \frac{\partial f_{vg}}{\partial \Phi} - \frac{\partial}{\partial x}\frac{\partial f_{vg}}{\partial \Phi_x} - \frac{\partial}{\partial y}\frac{\partial f_{vg}}{\partial \Phi_y} - \frac{\partial}{\partial z}\frac{\partial f_{vg}}{\partial \Phi_z} \tag{42}$$

and considering $g = g(I(x,y,z)) = g(x,y,z)$, we obtain

$$\tilde{H} = g\frac{(1+\Phi_x^2+\Phi_y^2)\Phi_{zz}+(1+\Phi_x^2+\Phi_z^2)\Phi_{yy}+(1+\Phi_z^2+\Phi_y^2)\Phi_{xx}-2\Phi_x\Phi_z\Phi_{xz}-2\Phi_x\Phi_y\Phi_{xy}-2\Phi_y\Phi_z\Phi_{yz}}{(1+\Phi_x^2+\Phi_y^2+\Phi_z^2)^{3/2}} + \tag{43}$$

$$+ \frac{g_x\Phi_x+g_y\Phi_y+g_z\Phi_z}{(1+\Phi_x^2+\Phi_y^2+\Phi_z^2)^{1/2}},$$

Since the normal vector $\vec{\mathcal{N}} = \frac{(-\Phi_x,-\Phi_y,-\Phi_z,1)^T}{\sqrt{1+\Phi_x^2+\Phi_y^2+\Phi_z^2}}$, the steepest descent flow is

$$\frac{\partial \Phi}{\partial t} = g\frac{(1+\Phi_x^2+\Phi_y^2)\Phi_{zz}+(1+\Phi_x^2+\Phi_z^2)\Phi_{yy}+(1+\Phi_z^2+\Phi_y^2)\Phi_{xx}-2\Phi_x\Phi_z\Phi_{xz}-2\Phi_x\Phi_y\Phi_{xy}-2\Phi_y\Phi_z\Phi_{yz}}{1+\Phi_x^2+\Phi_y^2+\Phi_z^2} +$$

$$g_x\Phi_x + g_y\Phi_y + g_z\Phi_z$$

that corresponds to Eqn. 16.

11   Acknowledgements

References

[1] V.Caselles, F.Catte', T.Coll, F.Dibos, *A Geometric model for Active Contours*, Numerische Mathematik,Vol.66, pp.1-31,1993

[2] V.Caselles, R.Kimmel, G.Sapiro, *Geodesic active contours*, IJCV, Vol.22,N.1,pag.61-79,1997

[3] V. Caselles, R. Kimmel, G. Sapiro, and C. Sbert, Minimal surfaces based object segmentation IEEE Trans. on PAMI, 19(4):394-398, 1997.

[4] T.F.Chan, L.A.Vese, *Active Contours without Edges*, CAM Report 98-53, UCLA Dept. of Mathematics, Dec., 1998.

[5] M. P. Do Carmo, *Differential Geometry of Curves and Surfaces*, Prentice Hall, 1976.

[6] D.Gabor, *Theory of Communication*, J. Inst. Elect. Eng., Vol. 93, pp. 429-457, 1946

[7] M. Giaquinta, S. Hildebrandt, *Calculus of Variations I*, Springer-Verlag, Berlin,1996.

[8] R.L. Gregory, *Cognitive Contours*, Nature, Vol. 238, N.5358, pp 51-52, July 7,1972.

[9] B.M.ter Haar Romeny (Ed.), *Geometry driven diffusion in computer vision*, Kluwer (1994)

[10] G.Kanizsa, *Subjective Contours*, Scientific American, pp. 48-52, April 1976.

[11] G.Kanizsa, *Organization in Vision* Hardcover, 1979.

[12] G.Kanizsa, *Grammatica del vedere* Il Mulino, 1980.

[13] M.Kass, A.Witkin, D.Terzopoulos *Snakes: Active Contours Models*, IJCV, Vol.1,N. 4,pp.321-331,1988.

[14] R. Kimmel, R. Malladi and N. Sochen. "Images as embedded maps and minimal surfaces: Movies, Color, Texture, and Medical Images," *International Journal of Computer Vision*, Vol. 39(2), pp. 111-129, 2000.

[15] B. Julesz *Textons, the elements of texture perception, and their interactions*, Nature, Vol. 91 N.7, pp. 91-97, 1981.

[16] T.S. Lee, *Image representation using 2D Gabor-wavelets*, IEEE Transaction on Pattern Analysis and Machine Intelligence, Vol.18, N.10, pp. 959-971, 1996.

[17] R. J. LeVeque, *Numerical Method for Conservation Laws*, Birkhauser, Boston,MA,1992.

[18] R. Malladi and J. A. Sethian, "Image processing: Flows under Min/Max curvature and Mean curvature," *Graphical Models and Image Processing*, Vol. 38(2) pp. 127–141, March 1996.

30

[19] J. Malik, S. Belongie, T. Leung, and J. Shi, *Contour and Texture Analysis for Image Segmentation*, in Perceptual Organization for Artificial Vision Systems, K.L. Boyer and S. Sarkar, editors. Kluwer Academic Publishers, 2000.

[20] J. Malik, S. Belongie, J. Shi, and T. Leung *Textons, Contours and Regions: Cue Combination in Image Segmentation* Int. Conf. Computer Vision, Sept 1999, Corfu, Greece

[21] R. Malladi, J. A. Sethian, B. Vemuri, *Topology independent shape modeling scheme*, SPIE Proceedings on Geometric Methods in Computer Vision II, San Diego, 1993, pp. 246-258.

[22] R. Malladi, J.A. Sethian, B.C. Vemuri, *Shape Modeling with Front Propagation: A Level Set Approach* IEEE Transactions on Pattern Analysis and Machine Intelligence, Vol.17, N.2, February 1995.

[23] R. Malladi and J. A. Sethian, "A real-time algorithm for medical shape recovery," in *Proceedings of ICCV'98*, pp. 304–310, Mumbai, India, January 1998.

[24] D. Marr, *Vision*, W.H. Freeman & Co., San Francisco, 1982

[25] D. Mumford, J. Shah, *Optimal Approximations by Piecewise Smooth Functions and Associated Variational Problems*, Communications on Pure and Applied Mathematics, Vol. XLII, pp. 577-685, 1989

[26] D. Mumford, *Elastica and Computer Vision* Algebraic Geometry and Its Applications, Chandrajit Bajaj (ed.), Springer-Verlag, New York, 1994.

[27] S. Nishikawa, R. Schoen, *Geometric Variational Problems*, Springer-Verlag, Tokyo, 1996.

[28] S. Osher, J.A. Sethian, *Front Propagating with Curvature Dependent Speed: Algorithms Based on Hamilton Jacobi Formulation*, Journal of Computational Physics, Vol. 79, pp.12-49, 1988

[29] P. Perona, J. Malik, *Scale space and edge detection using anisotropic diffusion*, In Proc. IEEE Computer Society Workshop on Computer Vision (1987)

[30] P.Perona, *Deformable kernels for early vision*, IEEE Transactions on Pattern Analysis and Machine Intelligence, Vol.17, N.5, pp. 488-499, 1995.

[31] A. Sarti, R. Malladi, J. A. Sethian, *Subjective surfaces: A Method for Completion of Missing Boundaries*, in the Proceedings of the National Academy of Sciences, Vol. 97(12), pp. 6258–6263, June 2000.

[32] A. Sarti, K. Mikula, F. Sgallari, *Nonlinear multiscale analysis of 3D echocardiographic sequences*, IEEE Transactions on Medical Imaging, Vol. 18, n. 6, pag. 453-466, June 1999

[33] A. Sarti and R. Malladi, *A geometric level set model for Ultrasound image analysis*, LBNL-44442, Lawrence Berkeley National Laboratory, October 1999; to appear in *Geometric Methods in Bio-Medical Image Processing*, Ed. R. Malladi, Springer Verlag, 2001.

[34] A. Sarti, C. Ortiz, S. Lockett, R. Malladi, *A unified geometric model for 3D confocal image analysis in cytology*, in IEEE Transactions on Biomedical Engineering, Vol. 47(12), pp. 1600–1609, December 2000.

[35] A.Sarti, R.Malladi, J.A. Sethian, *Elastic subjective surfaces* in preparation.

[36] E.Saund, *Perceptual Organization of Occluding Contours Generated by Opaque Surfaces* CVPR, 1999

[37] J. A. Sethian, *Curvature and the Evolution of Fronts*, Comm. Math. Phys., 101:487–499, 1985.

[38] J. A. Sethian, *Numerical Methods for Propagating Fronts*, in Variational Methods for Free Surface Interfaces, Eds. P. Concus and R. Finn, Springer-Verlag, NY, 1987.

[39] J. A. Sethian, *Level Set Methods and Fast Marching Methods*, Cambridge University Press, 1999

[40] N.Sochen, R.Kimmel, R.Malladi, *A General Framework for Low Level Vision*, IEEE Transactions on Image Processing, Vol. 7, N. 3, March 1998.

[41] L.R.Williams, D.W. Jacobs, *Stochastic Completion Fields: A Neural Model of Illusory Contour Shape and Salience*, Neural Computation, Vol.9, N.4,pp.837-858,1997.

[42] L.R.Williams, D.W. Jacobs, *Local Parallel Computation of Stochastic Completion Fields*, Neural Computation, Vol.9, N.4,pp.859-881,1997.
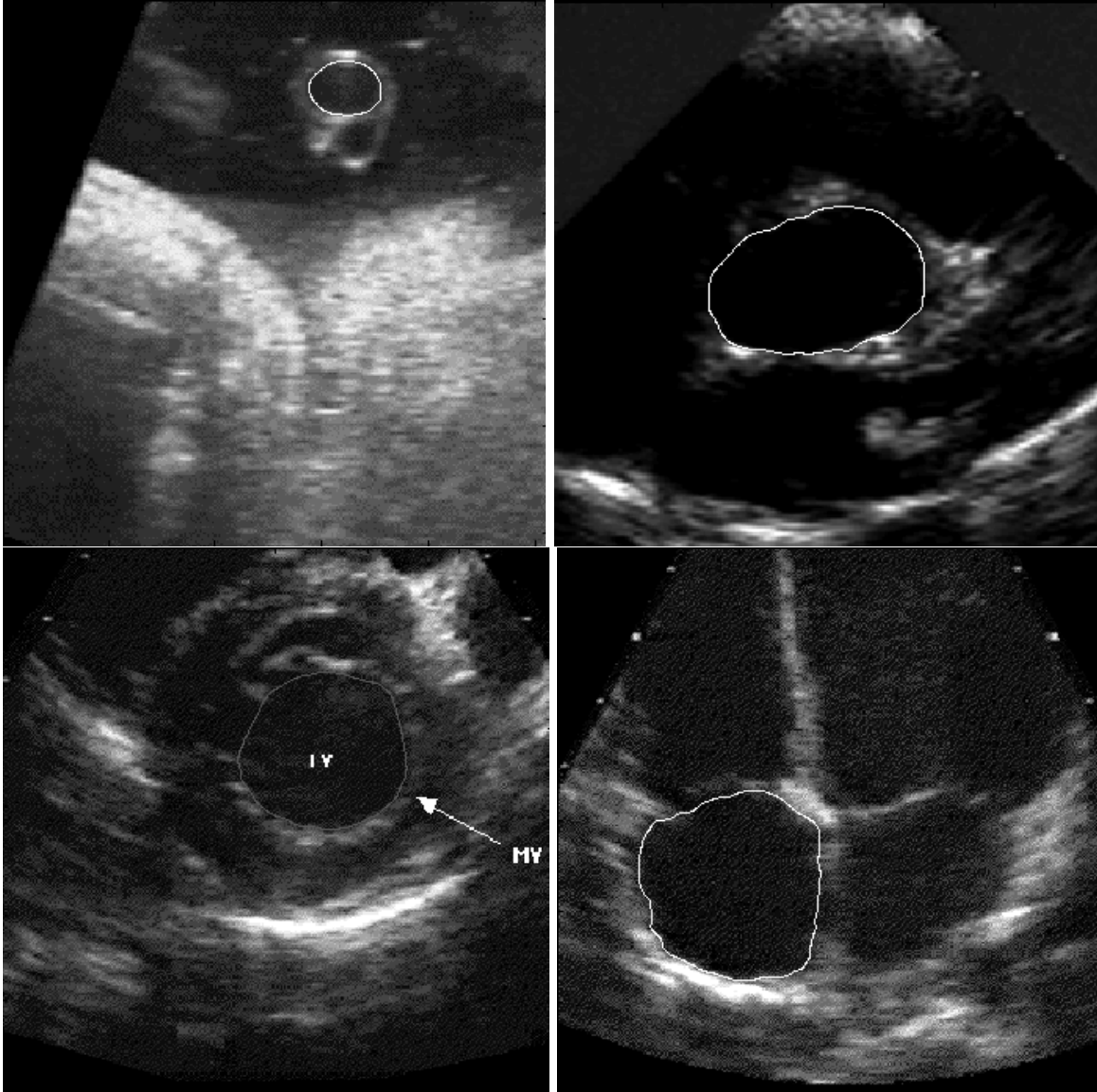
Figure 15: Segmentation of echographic images: in all the examples large parts of the boundaries are missing and modal completion is needed. Fetal cord echography (upper left), left ventricular chambers (upper right and bottom left) and left atrium (bottom right) are segmented.
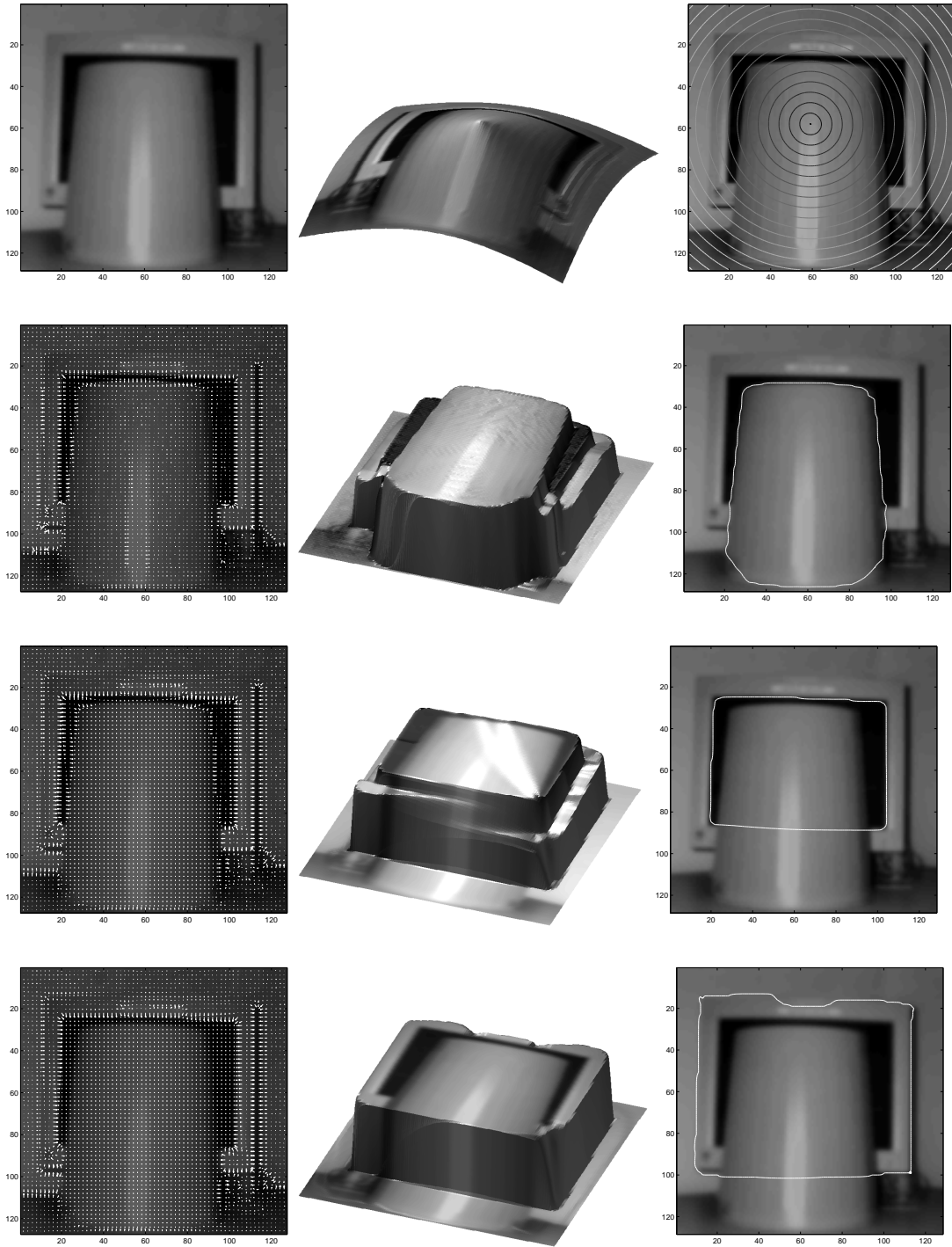
Figure 16: Extraction of partially occluded computer screen and computer monitor shapes from an image.
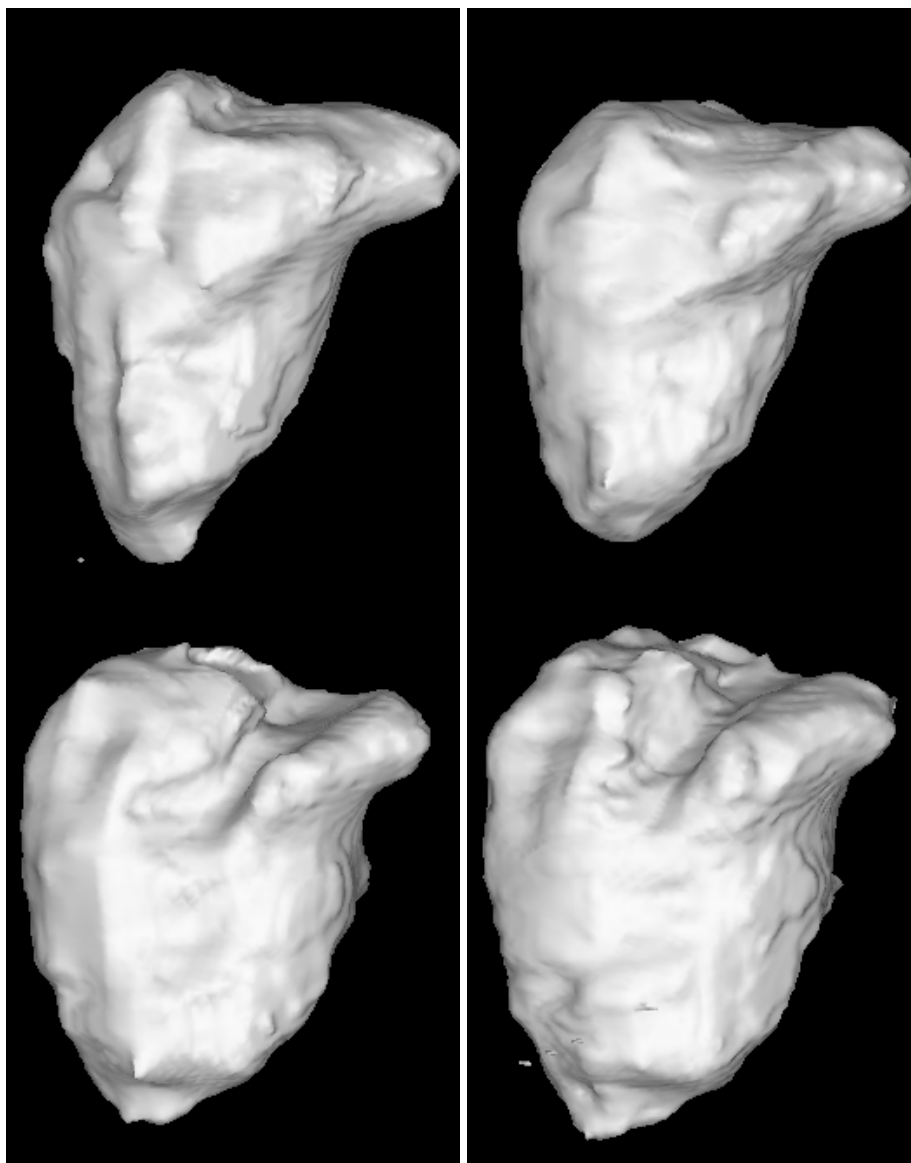
Figure 17: Extraction of the left ventricular chamber from a 3D ecocardiographic sequence.

Figure 18: 3D fetal echography segmentation.